Tunable plasmonic colours by atomic layer deposition of alumina

Jean-Michel Guay[1,4,*], Antonino Calà Lesina[1,3,4,*], Graham Killaire[1], Peter G. Gordon[5], Choloong Hahn[3,4], Sean T. Barry[5], L. Ramunno[1,4], P. Berini[1,3,4], A. Weck[1,2,4]
[1]*Department of Physics, University of Ottawa, 150 Louis-Pasteur, ON, K1N 6N5, Canada*
[2]*Department of Mechanical Engineering, University of Ottawa, 161 Louis Pasteur, ON, K1N 6N5, Canada*
[3]*School of Electrical Engineering and Computer Science, University of Ottawa, Ottawa, Canada*
[4]*Centre for Research in Photonics, University of Ottawa, Ottawa, Canada*
[5]*Department of Chemistry, Carleton University, Ottawa, ON, K1S 5B6, Canada*
**jguay036@uottawa.ca; Antonino.Calalesina@uottawa.ca*

Abstract: We report the tuning of plasmonic colours on silver by controlling the thickness of alumina films deposited via atomic layer deposition. The colours are observed to shift with increasing alumina film thickness. Colour palettes produced with periodic topographical features are observed to recover their original vibrancy and Hue range after the deposition of a film thickness of ~ 60 nm while colours devoid of such topographical features are observed to gradually fade and their colour intensities are never recovered collapsing into a small visually unappealing region of the LCH color space. Analysis of the surfaces identifies the periodic topographical features as responsible for this behavior. Finite-difference time-domain simulations of flat and sine-modulated surfaces covered with nanoparticles and covered by a conformal alumina film were conducted to unravel the role played by the ALD thickness on the colour formation, where colour rotations and recovery were also observed. The coloured surfaces were evaluated for applications in colourimetric and radiometric sensing showing large sensitivities of up to 3.06/nm and 3.19 nm/nm, respectively. The colourimetric and radiometric sensitivities are observed to be colour dependent.

Keywords: Metal Colourization, Plasmonic colouring, Nanostructures, Nanoparticles, Thin Films, Colour sensors, Computional Nanophotonics

1 Introduction

Plasmonic devices based on the unique optical properties of metallic nanoparticles have been a hot topic in the last decade, casting a wide net of promising applications in fields such as chemical and biomedical sensing,[1-5] photochemistry,[6-8] colouring[9-17], and surface-enhanced spectroscopy[18, 19]. Localized surface plasmon resonances (LSPR) are due to collective oscillation of the free electrons when exposed to optical radiation and are sensitive to the shape and size of the nanoparticles, the proximity of any surrounding nanoparticles and the refractive index of the local surrounding medium.[20-22] The use of plasmonic surfaces in sensing applications exploits the latter for the detection of target species due to the sensitivity of the LSPR to slight changes in the local refractive index. Research on optimizing the sensitivity of the plasmonic surfaces by seeking the largest possible LSPR shift has been an important driver in the development of plasmonic surfaces. Researchers have explored the fabrication of nanowires,[23] nanoshells,[24, 25] nanodisks[26] and other distinctive shapes and arrangements[27] to achieve the best LSPR sensor. Typical fabrication methods of such structures include lithography[28,14,29,30,31] and the growth of nanoparticles via chemical means.[32] While nanoimprint lithography[14,31] has promising scale-up potential, the initial step of mold fabrication is lengthy and often limited to small surface areas.

Recent advances in ultrafast laser technology and the creation of single step plasmonic surfaces via fast direct laser writing[11,10,9] of large surface areas[12,33] shows great promise for increasing production and cutting down on the fabrication time and cost of plasmonic devices. Additionally, compared to the ordered surfaces commonly fabricated using lithographic methods, surfaces coloured by ultrafast lasers are random. For colouring applications, it means that, under certain conditions, these surface do not exhibit angle-dependent colours typical of ordered surfaces.[12] However, using different laser parameters, the exposure of metals to laser light can also result in angle-dependent colours via the creation of laser-induced periodic surface structures (LIPSS)[9] that originate from the interference of the incoming light and a surface scattered wave.[34, 35] Recently, Guay *et al*.[36] demonstrated that these LIPSS combined with nanoparticles enhances plasmon resonances and could be tuned via different laser burst arrangements. Colour arising from light

interacting with LSPRs on noble metals is sensitive to the local environment so colour changes can be monitored in colourimetric[32] sensor applications.

In this paper, we report the tuning of plasmonic colours on the surface of laser-machined silver by varying the thickness of an alumina layer deposited thereon by atomic layer deposition. The colour palettes investigated are for burst and nonburst colouring methods.[12,37] We observed with increasing alumina thickness a broadening of the spectrum of the burst colours and witnessed an initial fading of the colours followed by the recovery of the original colour saturation, unique to the burst colours. Finite-difference time-domain (FDTD) simulations were conducted to understand the role of the ALD alumina layer on the nonburst and burst surfaces, which are modelled as a flat surface and a sine-modulated surface, respectively. FDTD simulations identifies the difference in behavior between burst and nonburst coloured surfaces to originate from the LIPSS that are unique to burst and enables grating-coupling. We also report sensitive colourimetric and radiometric sensors from the direct colouring of silver surfaces using a picosecond laser. The sensitivity of coloured silver surfaces is tested by the deposition of different alumina thicknesses via atomic layer deposition (ALD).

2 Experimental Methods

The silver surfaces were coloured by exposing large areas of the samples to laser irradiation by raster scanning the surfaces in a unidirectional top to bottom fashion (Fig. 1). The machining of the surfaces was carried out using a wavelength of 1064 nm emitted by a Duetto mode-locked laser (Nd:YVO_4, Time Bandwidth® Products) outputting 10 ps pulses. Two laser colour marking schemes are investigated, the 'burst mode' composed of a train of closely time-spaced pulses and the standard 'nonburst mode'. The colouring of silver using these two marking techniques is described in previous work[12,33,17]. The time separation between each of the pulses within the burst train is governed by the oscillator and is set to t_{ib} = 12.8 ns. A selection of 1 to 8 pulses within a laser burst can be selected and the energy distribution among the pulses can be adjusted using Flexburst™. The burst pattern (*i.e.* energy distribution) used to create the colours is shown in Fig. 1 (B). The repetition rate, $f = 1/T_b$, of the laser was set to 25 kHz using a pulse picker of 2 for the burst colours, and 50 kHz for the nonburst colours. After going through the XY galvanometric mirrors (TurboScan 10, Raylase), the light was focused onto the silver surface using an F-theta lens (f = 254 mm, Rodenstock). For accurate focusing, the surface of a sample was located using a touch probe arrangement. The silver samples were of 99.99% purity with a diameter of 38 mm and a thickness of 3 mm. For machining, the silver samples were placed on a 3-axis stage with a translation resolution of 1 µm in the lateral and axial directions. The laser power was controlled by a user interface and monitored using a power meter (3A-P-QUAD, Ophir). The spot size was measured to be ~28 µm following the semi-logarithmic plot approach of the modified region following previous work[38].

The colours were quantified using a Konica Minolta CR-241 Chroma meter in the CIELCH colour space, 2 observer and illuminant C (North sky daylight). The instrument outputs LCH values of the measured colours; where L is Lightness, C is Chroma (*i.e.* colour saturation) and H is Hue (colour value associated with a 360° polar scale). The LCH values were converted to the XYZ tristimulus colour space using Matlab for the plotting of the Commission de l'éclairage (CIE) diagrams. The reflectance measurements were taken via an in-house setup comprising a spectrometer (CCS200, Thorlabs) and a cold LED source (MCWHF2, Thorlabs). The light was sent and collected via a fibre optic reflection probe bundle (RP28, Thorlabs).

The ALD of alumina was performed using a Picosun R150 thermal deposition tool. Trimethylaluminum (TMA, >98%) and distilled water were held at 18°C in stainless steel bubblers for all of the depositions on the silver surfaces. Purges and line flows used 99.998% N_2 (150 sccm for TMA, 200 sccm for water). For all the depositions, there were six initial 1 s pulses of TMA followed by a 30 s purge. After the initial cycle, pulses and purge times for TMA and water were 1 s and 90 s, respectively. The depositions were performed with the temperature of the chamber set at 60 °C. Additionally, Si (100) "witness" wafers were placed in the chamber to confirm the expected growth rate of the alumina films. The silver samples were placed on a stainless steel mesh during deposition in order to support the samples and ensure complete coverage.

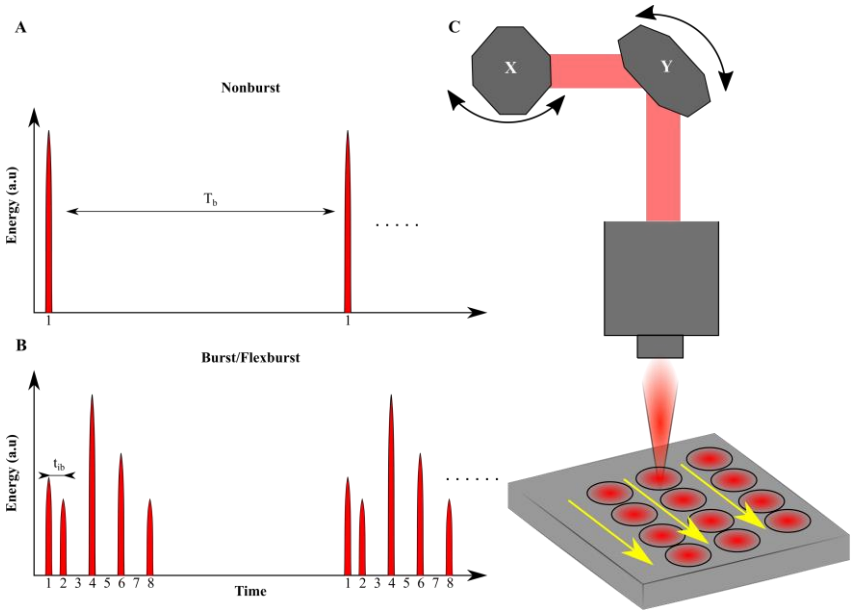

Fig. 1 | Experimental Setup. Schematic representation of the pulse energy distribution used for the (A) nonburst and (B) burst colours. The nonburst colours were written using a burst of 1 pulse (*i.e.* nonburst) with a laser repetition rate, f = 1/T_b, of 50 kHz while the burst colours were written using a burst pulse energy distribution shown in (b) with each pulse separated by 12.8 ns. The number of pulses within each burst can be set from 1 to 8. To increase the time separation between shots within the burst, the energy of pulses within the burst can be set to zero. (C) Schematic demonstrating the machining of samples using a top to bottom, unidirectional, raster scanning pattern.

The alumina films were probed by electron X-ray dispersive microscopy (EDX). The alumina layer thicknesses were estimated by entering the values of the EDX probe, voltage, takeoff angle, element, element k-ratio, and estimated density in the software GMFilm.[39] The EDX alumina thickness measurements were confirmed with, and the refractive index of the alumina film was obtained by ellipsometry (FUV-NIR, Horiba Uvisel) with an incident angle of 70° and measured over the spectral range of 235 – 2000 nm in steps of 5 nm. Grazing angle measurements were performed with an FT-IR spectrometer (Nexus 870, Thermo Nicolet) with the incident light hitting the surface of the sample at an angle of 80°.

3 Results and Discussion

3.1 Colourimetric response to the atomic layer deposition of alumina

In a previous study, a multi-layer coating method was developed to minimize morphological and colourimetric changes on the sample surface while protecting the surface against chemical attacks in order to target a specific industrial application.[33] The mechanism of island formation and film growth on the silver surface during ALD was discussed.[33] Here, a layer of alumina is deposited over pre-existing silver colours to investigate its effect on colour changes in order to compensate or predict the final image canvas. Fig. 2 is a side-by-side comparison of a full color palette (a) without and (b) with a 90 nm thick film of alumina deposited via ALD. The colours on the surface of the silver samples were obtained using the nonburst (top in Figs. 2(a) and 2(b)) and burst (bottom in Figs. 2(A) and 2(B)) laser colouring methods, discussed in a previous publication.[12,36] The nonburst and burst laser parameters used were a marking speed of 100 mm/s with a laser fluence of 5.73 J/cm^2, and 150 mm/s with a fluence of 12.12 J/cm^2, respectively. The different colours were obtained by changing the line spacing, L_s, between successive lines, controlling the density of nanoparticles re-deposited onto the metal's surface.[12]

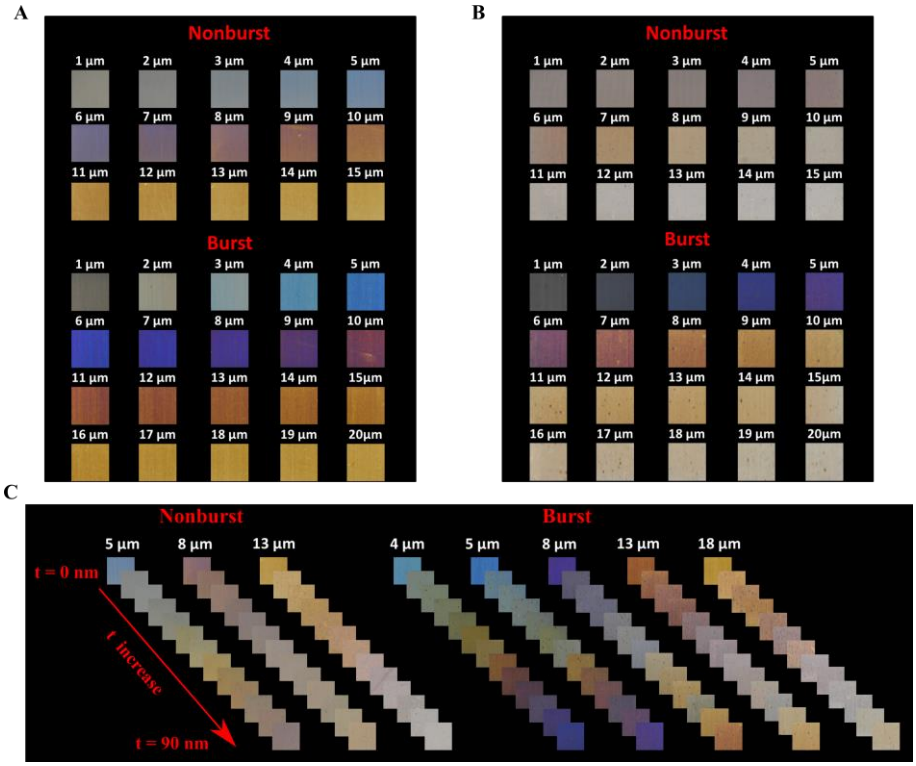

Fig. 2 | Colour evolution with alumina thickness. (A,B) Colour palettes obtained using the (top) nonburst and (bottom) burst laser colouring methods (A) before and (B) after the deposition of 90 nm of alumina. The different colours were obtained by changing the line spacing, L_s, in steps of 1 µm, creating squares of 4 x 4 mm^2 in area. The colours were written using a laser fluence of 5.73 J/cm^2 with a marking speed of 100 mm/s and a laser fluence of 12.12 J/cm^2 with a marking speed of 150 mm/s for the nonburst and burst colours, respectively. (C) Colour evolution with increasing alumina thickness from 0 to 90 nm in steps of ~ 7 nm.

From Figs. 2(A) and 2(B), the colors are observed to change significantly for both nonburst and burst colors following the application of the 90 nm layer of alumina. For the burst case, intense colours are still observed after deposition of the 90 nm alumina film. Conversely, for nonburst, the colours are observed to be grayish and lighter. In industrial applications where visual colours are wanted, a smaller change in colour (*i.e.,* ΔE) is preferred,[40] thereby conserving the vivid colour palette. Fig. 2(B), suggests that burst coloured surfaces are the preferred choice in applications where protective coatings or tagging agents are to be placed on the coloured surface. Conversely, in colourimetric sensing applications, large changes in colour are desired. Fig. 2(C) shows the evolution of colour with increasing alumina thickness in steps of ~ 7 nm for a few selected line spacings. Twelve identical colour palettes on twelve silver samples were placed in the ALD chamber and one sample was removed after each deposition of ~ 7 nm. The nonburst colours are observed to gradually lose their Chroma with increasing alumina thickness. Alternatively, for the burst case, the Chroma of the colours is mostly recovered at larger film thicknesses. Indeed, the burst colours are observed to rotate in Hue by almost 360° going from blue (H = 249.2) to purple (H = 291.4) with increasing alumina thickness (as discussed further below). Green colours can be distinctively observed during the colour transition with increasing ALD thickness, *e.g.* burst colours in Fig. 2(C) for the case L_s = 4 µm. Green colours with this direct laser colouring method have, in the past, been difficult to obtain.[12] Thus, the alumina layer can serve as a tuning element to obtain colours over a wider range of Hue values. For nonburst, only blue is observed to rotate in colour; however, the Chroma of the colours is significantly reduced and does not recover with increasing alumina thickness.

Fig. 3 shows (CIE) xy Chromaticity diagrams for nonburst and burst colours as the alumina film thickness increases. Initially, the area covered by the colours on the CIE diagrams for each of the colouring methods is observed to decrease with increasing alumina thickness. In a CIE xy Chromaticity diagram, the Chroma (*i.e.* saturation) increases from the centre outwards. For burst, the area covered by the colours extends to cover more of the green region after the initial deposition of alumina. Additionally, the decrease in covered area was observed up to a thickness of 55 nm before gradually recovering up to the maximum applied thickness of 90 nm. The reduction in the area is caused by a reduction in the Chroma. The point of recovery for the burst colours appears to occur around ~ 55 nm of alumina. At 90 nm, the

Chroma is largely recovered. In the nonburst case, the Chroma decreased and never recovered, yielding colours that are mostly gray. Additionally, the area spanned by the colours continuously decreased with increasing thickness, collapsing into a small region of the CIE diagram.

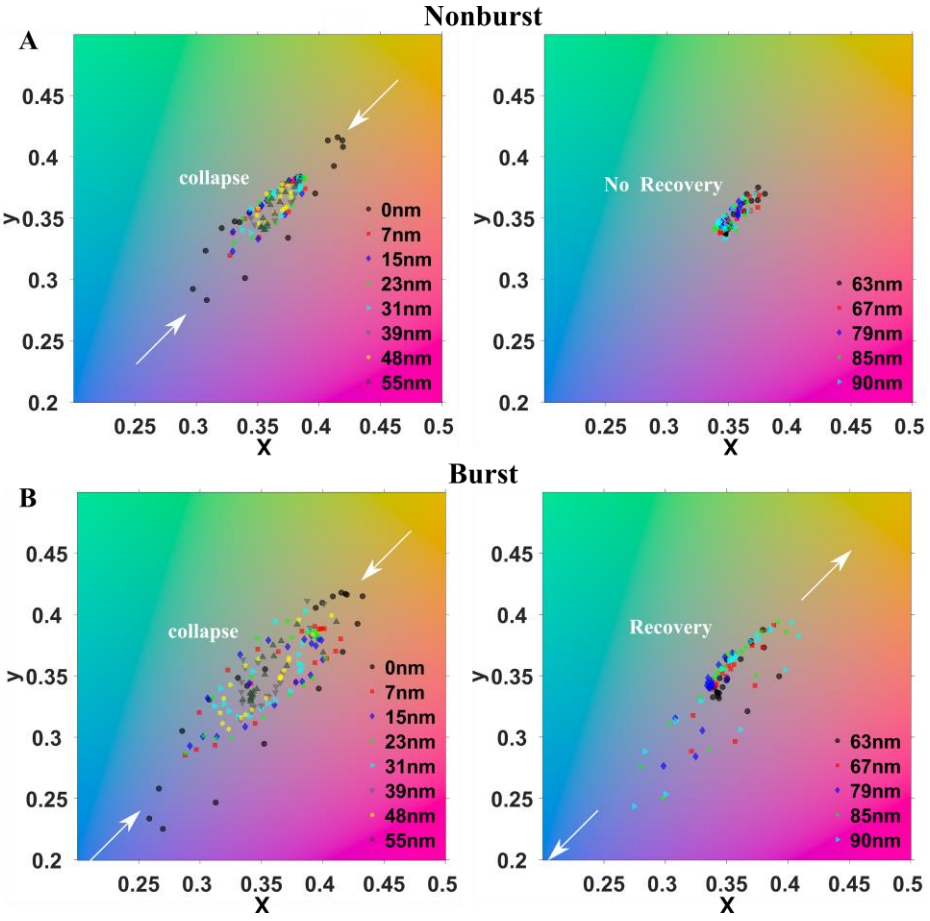

Fig. 3 | CIE of colours with increasing ALD thickness. CIE xy Chromaticity diagrams showing evolution of the (A) nonburst and (B) burst colours with increasing ALD thickness. The area on the CIE diagram spanned by the nonburst colours is observed to collapse with increasing alumina thickness. For the burst colours, the area spanned is observed to recover after 55 nm of alumina.

Fig. 4 shows polar plots of Hue (θ) versus total accumulated fluence (r) for the nonburst and burst colours with increasing alumina thickness. For the nonburst colours, the evolution of the Hue values is observed to follow a brushing/sweeping motion (red arrow) with increasing alumina thickness. The brushing/sweeping motion initially moves to the right, until the thickness of 55 nm, before reversing direction to sweep left. At the thickness of 90 nm, the Hue values have almost recovered their original values. It should be pointed out that throughout the motion in the nonburst case new Hue values are never added. For burst colours, however, the evolution of the Hue values is different, exhibiting a counter-clockwise rotation with increasing alumina thickness. This counter-clockwise motion allows access to the green Hue range (90-150°) that is usually very difficult to achieve with direct laser machining alone. A Chroma gain of up to 61% can be observed in the green colour region (H = 90 to 150) compared to the best green colours obtained to date.[12] Hence, the burst colours are tunable to cover Hue values outside the normal range depending on the thickness of the alumina layer. Similarly, to the nonburst colours, the original Hue range is mostly recovered after deposition of 90 nm of alumina, with a distinctive crossing point at 55 nm.

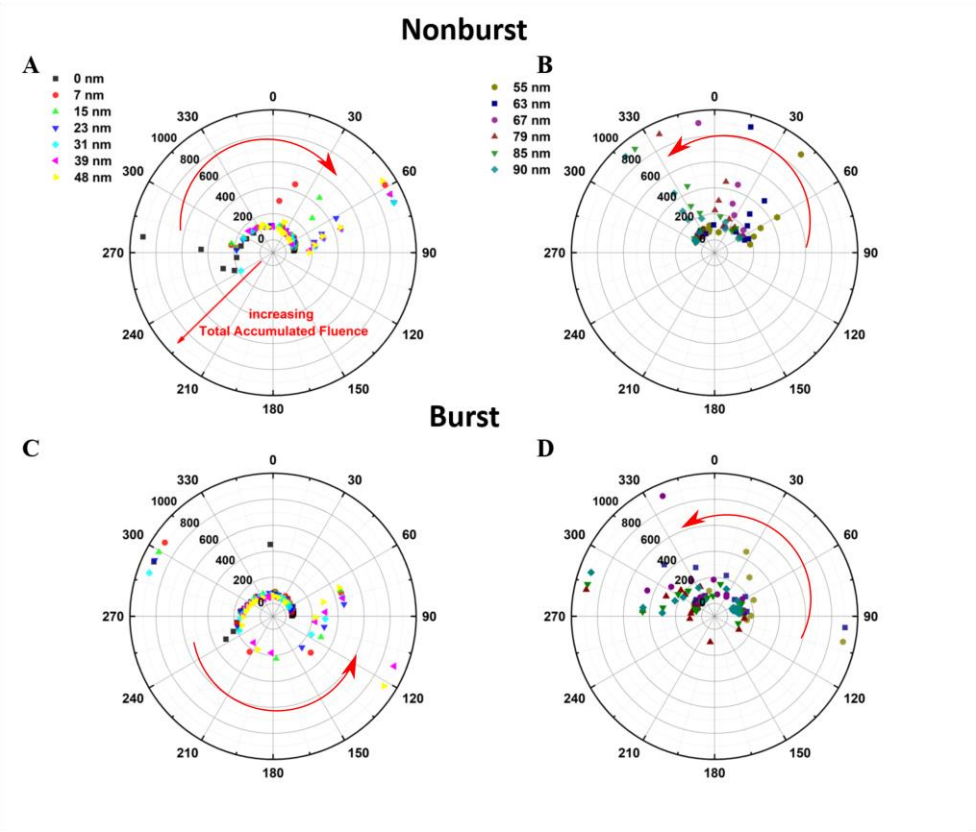

Fig. 4 | Hue values of colours with increasing ALD thickness. Polar plots of Hue (θ) versus total accumulated fluence (r) for the (A,B) nonburst, and (C,D) burst colours with increasing alumina thickness. The different points in the plots represent the Hue range of the colour palette for a certain alumina thickness. The evolution and displacement of the Hue values with increasing alumina thickness is displayed by the red arrow.

It is widely known that changes to the local permittivity can be used to tune the plasmonic response of nano-textured surfaces.[22] While both colouring methods recovered their original Hue values (Fig. 4), recovery of the Chroma values was observed solely in the burst case (Fig. 3). However, since the burst and the nonburst surfaces have similar nanoparticle statistics[17] and alumina film thicknesses it would be expected that both should present a similar behavior. The only difference between the two lies with the underlying topography unique to the burst surfaces.[17] The LSFL and HSFL structures found on the burst coloured surface is the key to understanding the different behaviors with increasing alumina thickness. The structures would serve to increase the area covered by the nanoparticles and cause field-enhancement in the crevices, both increasing absorption.[17] Furthermore, while the coloured surfaces have been previously shown to be sensitive to heat and to irreversibly degrade with prolonged heat exposure,[33] the recovery of the colours with increasing film thickness rules out the heat as being responsible for the colour change.

In a colouring application, the passivation of the nonburst coloured surfaces would necessitate the deposition of a thickness lower than 7 nm in order to minimize the change in the colours and retain the original visual appeal of the colours, see Fig. 3. For burst, the alumina layer could either be below 7 nm or around 90 nm, see Fig. 3(B), the latter providing better passivation. In a previous publication it was demonstrated that alumina films deposited at 60 °C required a minimum layer thickness of 57 nm in order to protect coloured surfaces against chemical attack.[33]

Fig. 5 shows reflectance measurements of selected coloured squares with different alumina thicknesses. The reflectance measurements in Fig. 5 are for blue (L_s = 5 µm) and purple (L_s = 8 µm) colours prior to the deposition of the alumina film, produced using the nonburst and burst colouring methods.[12] The features in the reflectance curves appear to follow similar trends for the different colours. The burst colours showed more defined features and larger variations between the peaks and valleys, explaining the higher Chroma. With increasing film thickness various features in the reflectance spectra emerge or shift (dotted lines); some of these features being more active than others. The shifts in the peaks/troughs are observed to be colour dependent with the blue colours being the most active.

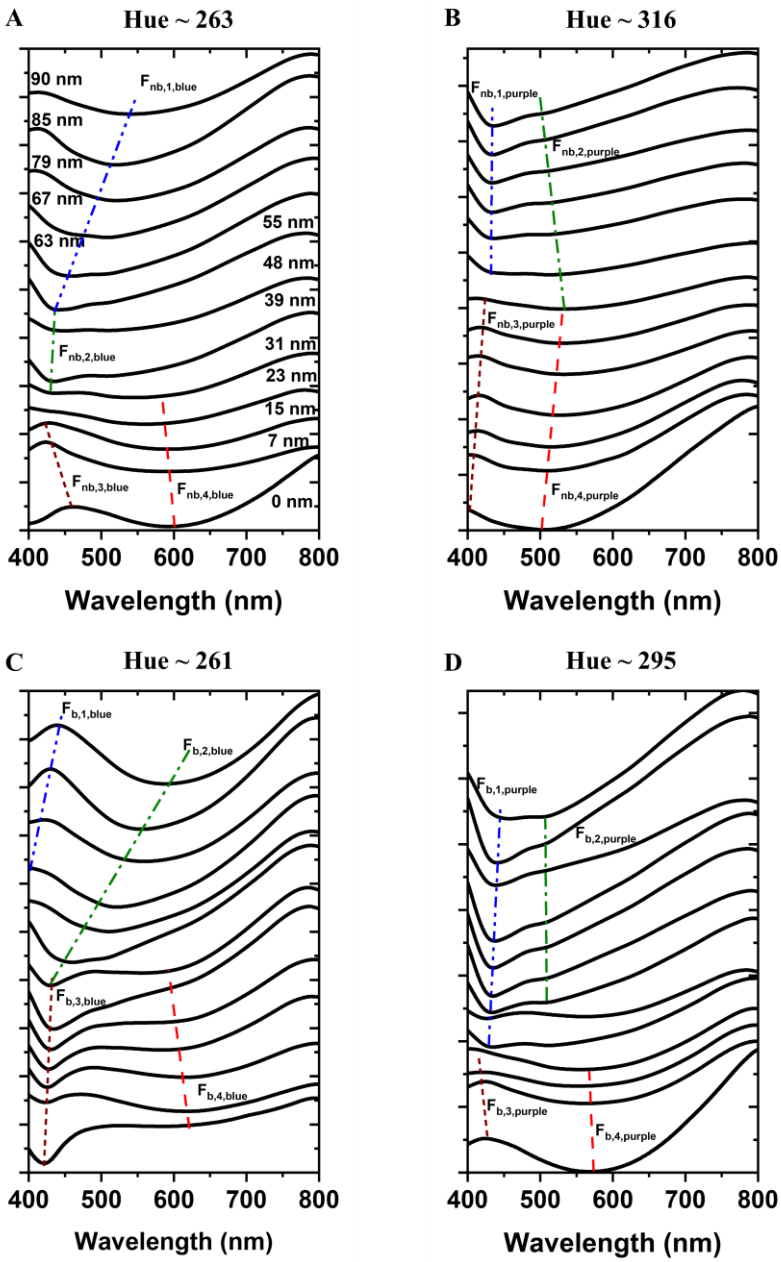

Fig. 5 | Experimental reflectance spectra. Measured reflectance spectra with increasing alumina thickness for blue (left) and purple (right) colours written using (A), (B) the nonburst method (laser fluence of 5.73 J/cm^2, marking speed of 100 mm/s), and (C), (D) the burst method (laser fluence of 12.12 J/cm^2, marking speed of 150 mm/s). The blue colours were written using a line spacing of 5 µm and the purple colours were written using a line spacing of 8 µm. The shifting of spectral features with increasing alumina thickness is tracked with straight lines of different line styles (as a guide to the eye). The original Hue values are identified at the top of each panel.

3.2 Surface Chemical Analysis

FTIR measurements of coated surfaces, plotted in Fig. 6(A), clearly show the presence of Al_2O_3 on the surface of coloured silver. A peak at 952 cm^{-1} representative of Al-O vibration can be distinguished.[41,42] The alumina film was deposited at the low temperature of 60 °C in order to limit any colour change caused by thermal damage to the nanostructure during deposition (the melting temperature of small silver nanoparticles is lower than the bulk[43,44]). Silicon witness wafers were placed in the deposition chamber and one was removed systematically at the same time as a silver sample. The thickness of each film was measured using a multi-point measurement approach and determined using

GMRFilm software using K-ratios from electron dispersive X-ray spectroscopy (EDS).[39] The thickness of each film was also determined by ellipsometry measurements, along with their refractive index dispersion. Fig. 6(B) compares the refractive index of thin films of Al_2O_3 deposited via pulsed laser deposition[45] to the refractive index of our Al_2O_3 layers deposited by ALD on our witness wafers. The thicknesses obtained by ellipsometry on the silicon witnesses are in agreement with the EDX measurements obtained on the silver samples. In every case, the measured refractive index of the deposited films is lower than the films measured by Boidin et *al.*[45] The low refractive index of our alumina is explained by the low deposition temperature used.[46] The refractive index of the deposited alumina layer can be modified by changing the deposition temperature: *e.g.*, see the case for 250 cycles deposited at 100 °C in Fig. 6(B).

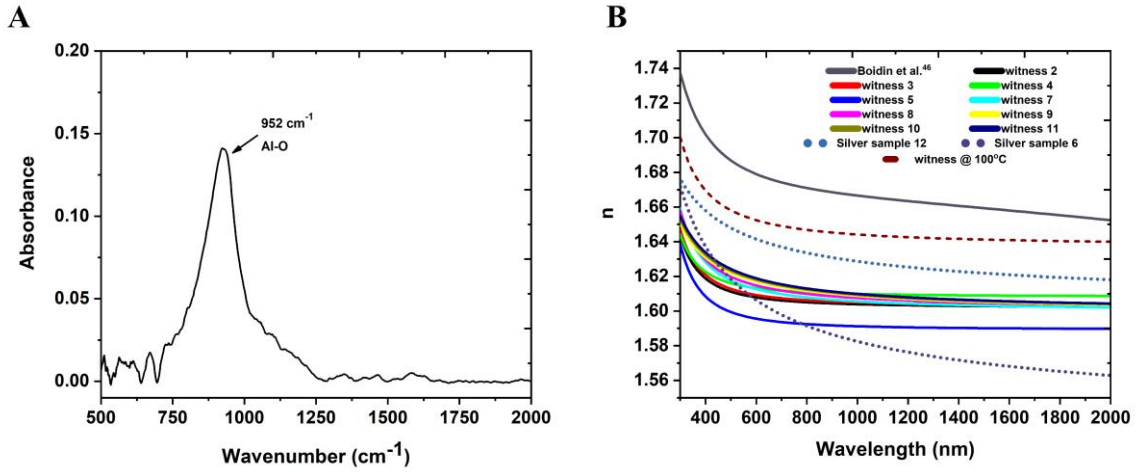

Fig. 6 | Alumina film measurements. (A) FTIR measurement of a coloured silver sample covered with an alumina film deposited by ALD. The peak at 952 cm^{-1} can be attributed to Al-O vibrations. (B) Plot comparing the refractive index of amorphous Al_2O_3 as measured by Boidin et al.[45] and the refractive index of the deposited films measured by ellipsometry on the witness silicon wafers and the two silver samples. The difference in the refractive index is attributed to the low temperature deposition of the alumina film producing lower density and porous films.

3.3 Numerical simulations

Based on AFM scans and SEM images of the coloured surfaces, a computational model was designed and the FDTD method was applied to calculate the reflectance in the optical regime.[12] This model includes a metallic surface (both flat and topographical surfaces are considered), supporting metallic nanoparticles, covered by a conformal coating of alumina. For burst surfaces, two characteristic spatial periods were identified for ripples on the surfaces, *i.e.*, $L_p \sim 1000$ nm (LSFL) and $L_p \sim 200$ nm (HSFL), with HSFL running perpendicular to the LSFL.[36] In simulations the ripples are modelled by a sine-modulated surface in the x-direction, *i.e.*, by using the function $f(x,z) = A \cdot sin(2\pi x/L_p)$, where L_p is the spatial period of the sinusoid and A its amplitude, as shown in Figs. 7(A) and 7(B) for LSFL and HSFL, respectively. The silver NPs of radius $R_m = 35$ nm are arranged on this surface following a square lattice with centre-to-centre distance D_m. The NPs are embedded into the surface by 30% of their radius in the direction normal to the surface. The model is 3D, and periodic boundary conditions are applied over a period L_p in the x-direction and over a period D_m in the z-direction. An alumina layer of thickness of t_{ALD} is assumed conformal[47] to the surface and the nanospheres, and its optical parameters are modelled in FDTD by fitting the data in Fig. 6(B) (case of 250 cycles at 100 °C) to a Lorentz model. We consider a y-propagating plane wave excitation (normal incidence) for two cases of polarisation (x- and z-polarization) because the sine-modulation makes the model polarization-dependent. The Ag is modelled using the Drude model with 2 critical points (Drude+2CP).[48] A space-step of 0.5 nm was used to discretize the simulation domain.

In Figs. 7(A) and 7(B) we show the electric field magnitude for the x-polarized excitation at $\lambda_0 = 500$ nm for $L_p = 1000$ nm ($D_m = 100$ nm, $A = 100$ nm, $t_{ALD} = 50$ nm) and for $L_p = 200$ nm ($D_m = 100$ nm, $A = 40$ nm, $t_{ALD} = 50$ nm), respectively, where the geometric parameters are highlighted, *i.e.*, D_m, A, t_{ALD} and L_p. Figs. 7(A) and 7(B) reveals two

plasmonic resonant modes for nanoparticles distributed on the surfaces with topography, LSFL and HSFL, respectively. We also observe that the ALD layer is thick enough to confine the near-field in the vicinity of the nanoparticles. For the $L_p = 1000$ nm case, the field distribution as a function of λ_0 is shown in Media 1 in steps of 10 nm. Fig. 7(A) is extracted from Media 1 and shows a surface wave propagating in the x direction directly above the ALD layer due to grating coupling.

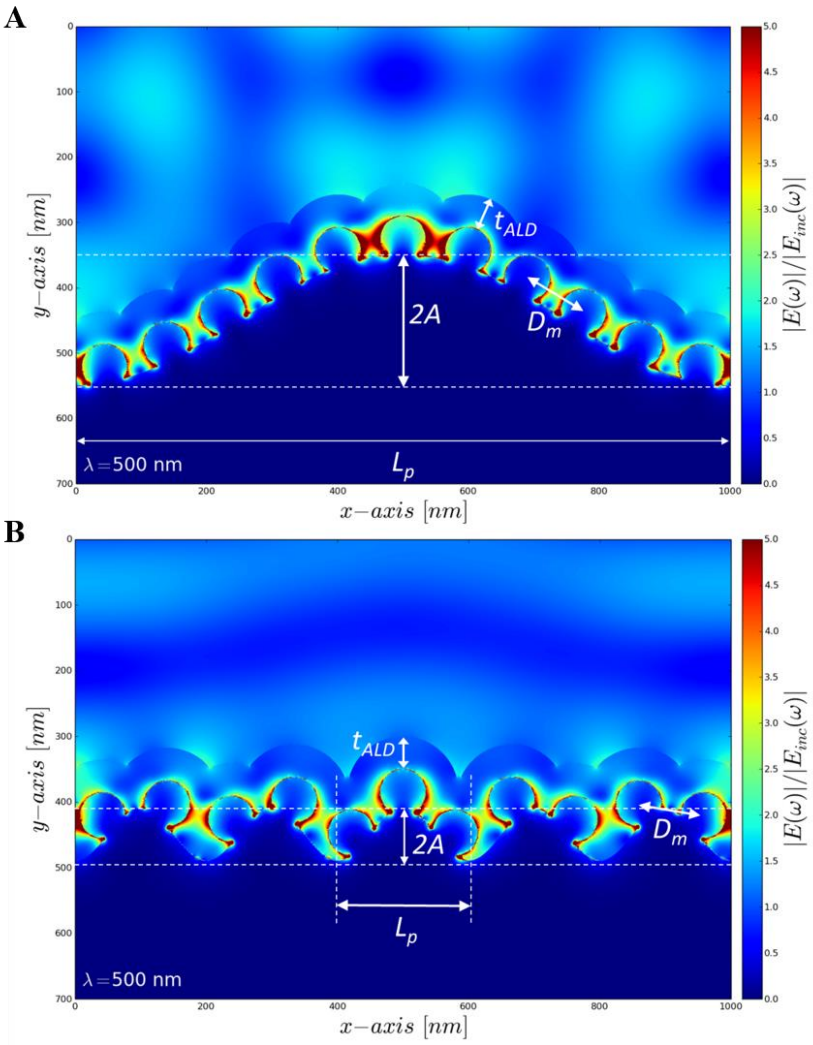

Fig. 7 | Simulation setup and computed near-field for NPs on sine-modulated surfaces covered with a film of alumina. Electric field (magnitude) distribution at $\lambda_0 = 500$ nm under x-polarized excitation for (A) $L_p = 1000$ nm, $D_m = 100$ nm, $A = 100$ nm, $t_{ALD} = 50$ nm, and (B) $L_p = 200$ nm (5 periods are considered in simulations), $D_m = 100$ nm, $A = 40$ nm, $t_{ALD} = 50$ nm. The xy plots are taken through the center of the spheres

In Media 2 and Media 3, we show the evolution of the electric field in the case of an x-polarized plane wave pulse interacting with the surface for $L_p = 1000$ nm, $D_m = 100$ nm, $A = 100$ nm, $t_{ALD} = 10$ nm and $t_{ALD} = 100$ nm, respectively; whereas in Media 4 and Media 5, we show the case of $L_p = 200$ nm, $D_m = 100$ nm, $A = 40$ nm, $t_{ALD} = 50$ nm and $t_{ALD} = 100$ nm. These movies reveal the complexity of the plasmonic resonances that occur when nanoparticles are arranged on a rippled surface and covered by a thin dielectric layer.

In Fig. 8, we show the evolution of the reflectance and the corresponding colour (rendered as the linestyle colour for each curve) in the non-burst case as t_{ALD} varies from 0 to 100 nm, and for $D_m = 75$ nm in Fig. 8(A), $D_m = 80$ nm in Fig. 8(B), $D_m = 85$ nm in Fig. 8(C), and $D_m = 100$ nm in Fig. 8(D). In the non-burst case ($A = 0$ nm), the NPs are arranged on a flat surface and their optical response is polarization independent. For t_{ALD} smaller than the gap size $g = D_m - 2R_m$, the ALD layer strongly affects the resonance condition because the gap is not fully filled. For example, for $D_m = 75$ nm

(Fig. 8(A)) the gap size is g = 5 nm, thus small increments of t_{ALD} between 1 and 4 nm produce a quick fill of the gaps between NPs and a rapid change in colour; this corresponds to increasing the optical thickness between nanoparticles and a transition from blue to yellow is observed, as previously reported[10]. Once the gaps are filled, there is little further change in the plasmonic resonances. The colour change as a function of t_{ALD} is then due to altered reflection by the multi-layer system and modified coupling by the grating. This can be observed in the reflectance curves of Figs. 8(A)-8(D) on the left and the right of the plasmonic resonance dip. For D_m = 80 nm (Fig. 8(B)) the initial violet colour (H = 334) goes through a rotation (magenta/orange) and recovers for t_{ALD} ~ 80 nm. For D_m = 85 nm (Fig. 8(C)) the initial light orange colour (H = 32) goes through a rotation (magenta/violet) and recovers for t_{ALD} ~ 40 nm. For D_m = 100 nm (Fig. 8(D)) we see that the initial yellow evolves through orange/red/brown/magenta/violet for increasing t_{ALD}. For D_m = 75 nm, no colour rotation and recovery is observed. In our chosen examples, the colour rotations and recovery qualitatively reproduce some of the trends observed in non-burst experiments, *e.g.*, blue-to-yellow add yellow-to-violet in left side of Fig. 2(C).

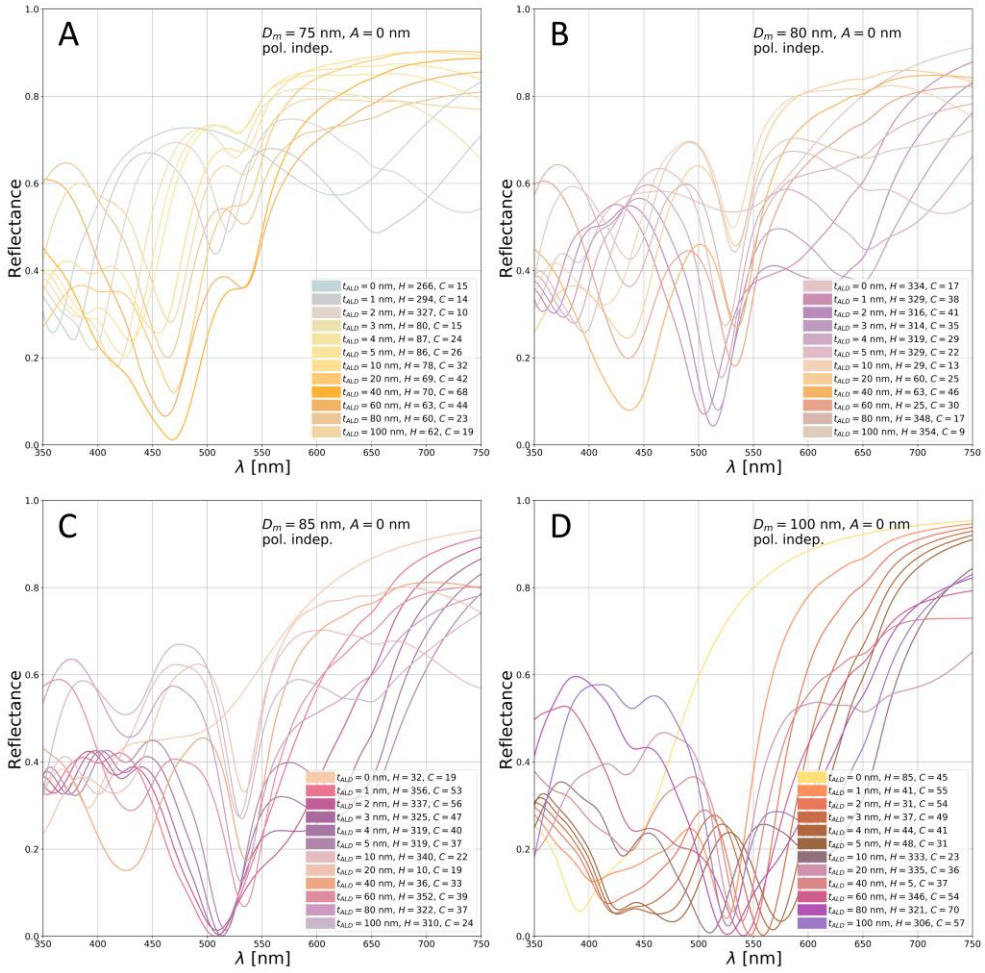

Fig. 8 | Computed reflectance spectra in the nonburst case. Reflectance and colour evolution (Hue and Chroma) in the non-burst case (A = 0 nm) as a function of t_{ALD} for (A) D_m = 75 nm, (B) D_m = 80 nm, (C) D_m = 85 nm, and (D) D_m = 100 nm. The lin-estyle colours were rendered by converting the reflectance spectra to a colour and using the associated RGB values.

In Fig. 9, we show the computed reflectance response as t_{ALD} varies from 0 to 100 nm in the burst case (A = 100 nm) for z-polarization (D_m = 75 nm in Fig. 9(A), D_m = 80 nm in Fig. 9(B), D_m = 85 nm in Fig. 9(C), and D_m = 100 nm in Fig. 9(D)) and x-polarization (D_m = 80 nm in Fig. 9(E) and D_m = 90 nm in Fig. 9(F)).

Figs. 9(A)-9(D) and Figs. 8(A)-8(D) show similar trends. The main differences in hue arise from the fact that the structures modelled in Fig. 9 contain narrowband features in the reflectance around λ_0~ 500 nm which enrich the colour palette. For x-polarized excitation (Figs. 9(E) and 9(F)), these features are due to grating-coupling with the sine-modulated surface. The grating-coupling response is complex due to the large amplitude A of the sine function, which

represents a strong perturbation leading to multiple dips in the reflectance, and new resonance conditions, such as out-of-plane resonances involving NPs arranged partially along the direction of propagation (y) of the exciting optical pulse. For z-polarized excitation, the presence of narrowband dips at $\lambda_0 \sim 500$ nm is counterintuitive, and they are probably due to resonances arising from the complex geometries that we are simulating. As in Fig. 9, similar features in the reflectance responses are observed for the situation of Fig. 7(B), *i.e.*, for L_p= 200 nm (not shown). In general, the presence of the ripples makes the colours without ALD more saturated,[36] whereas increasing t_{ALD} can be exploited as a technique to further extend the colour palette to Hues which are not accessible using plasmonic resonances only.[12] In Figs. 9(D) and 9(F), we note the presence of very saturated blue/magenta colours for high t_{ALD}, which is also observed in experiments (right side of Fig. 2(C)).

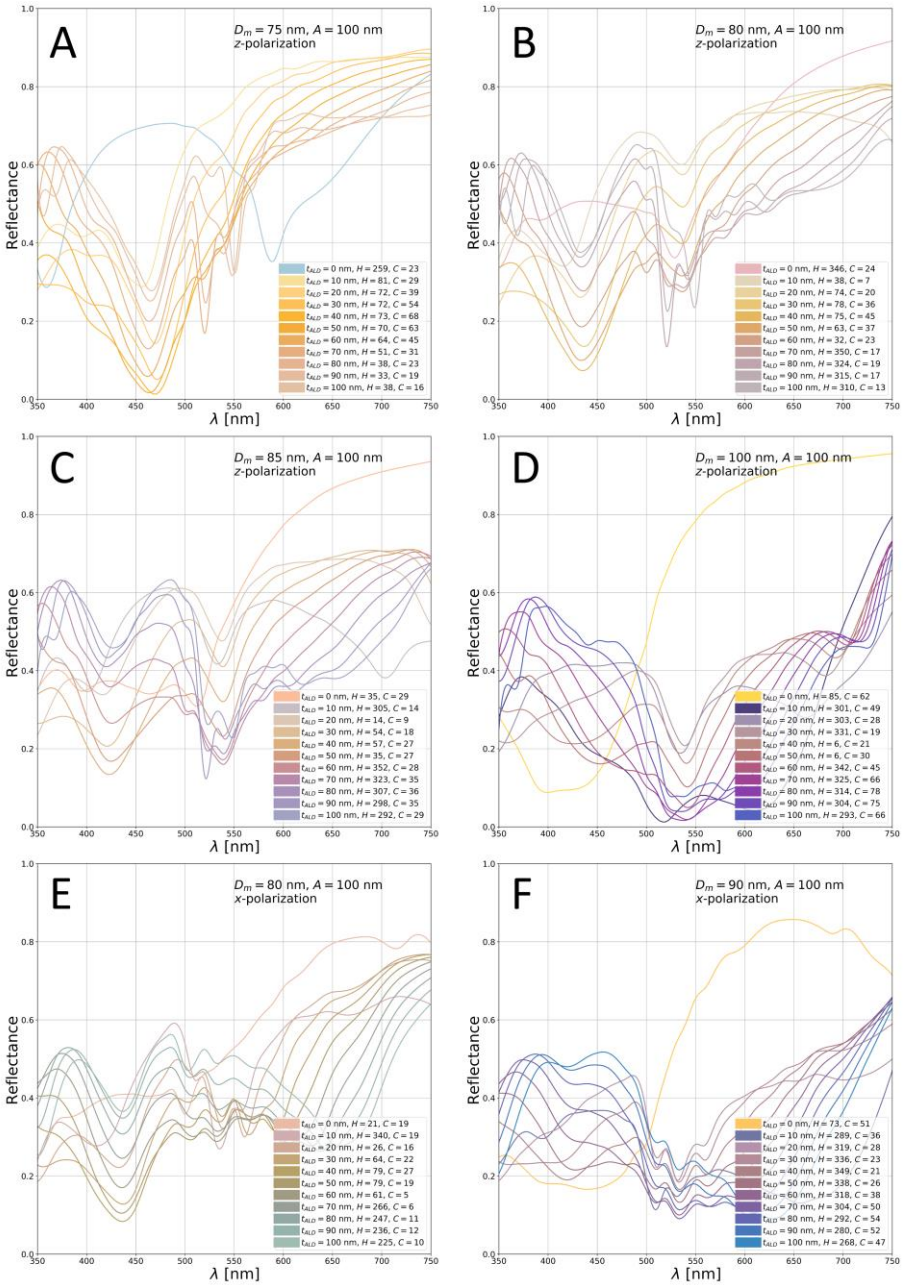

Fig. 9 | Computed reflectance spectra in the burst case for x- and z- polarized excitation. Reflectance and colour evolution (Hue and Chroma) in the burst case (A = 100 nm) as a function of t_{ALD}, for z-polarization with (A) D_m = 75 nm, (B) D_m = 80 nm, (C) D_m = 85 nm, (D) D_m = 100 nm, and for x-polarization with (E) D_m = 80 nm, (F) D_m = 90 nm. The linestyle colours were rendered by converting the reflectance spectra to a colour and using the associated RGB values.

3.4 Surface sensitivity

The visual differences in the colours and the changes observed in the reflectance spectra with increasing alumina thickness (Figs. 2(C) and 5) suggest that the surfaces could be used in colourimetric sensing applications (*e.g.*, colour change biosensors). The examine the potential for this application, we plot in Fig. 10 the change in colour ΔE versus Hue with increasing film thickness for nonburst and burst colours. The change in colour is defined by the following relation[40]:

$$\Delta E = \sqrt{(L_2 - L_1)^2 + (a_2 - a_1)^2 + (b_2 - b_1)^2} \quad (1)$$

where a and b are given as

$$a = C \times cos\left(\frac{2\pi H}{360}\right) \quad (2)$$

and

$$b = C \times sin\left(\frac{2\pi H}{360}\right) \quad (3)$$

L is Lightness, C is Chroma and H is Hue - the three components of the LCH color space. In Eq. 1, subscripts 1 and 2 are used to identify the colours before (1) and after (2) ALD coating.

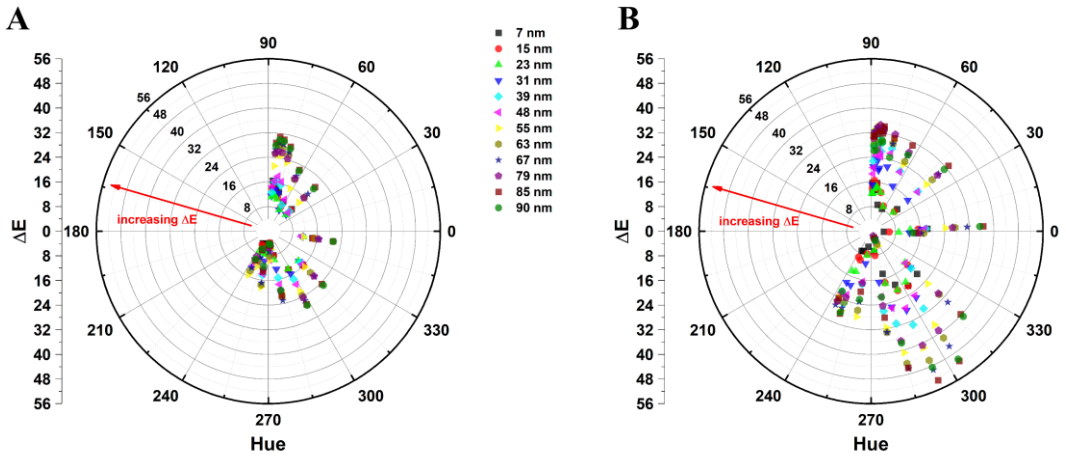

Fig. 10 | Colourimetric sensing response of the coloured surfaces. Polar plot of the change in colour (*i.e.* ΔE) versus Hue for the (A) nonburst and (B) burst colours with increasing alumina thickness. The change in colour, ΔE, increases radially outward as represented by the red arrow. The change in colour with alumina thickness is observed to be dependent on the initial Hue value.

ΔE ~ 1 is the minimum colour change that the human eye can discern.[40] A significant change in colour can be observed for both the nonburst and burst colours with increasing alumina thickness. The ΔE is observed to depend on the starting colour before deposition of the alumina film. In both cases, the most sensitive Hue region is in the purple colour range (H = 270 to 330). The sensitivity of the burst colours are observed to be higher in the blue (H = 210-270) and purple region (H = 270 to 330), by 96% and 75%, respectively, compared to the nonburst colours of the same Hue regions. The Increase in ΔE for the burst colours are believed to come from the periodic structures unique to the burst coloured surfaces. The ability to tune these structures with different burst arrangements[36] could potentially serve to increase their sensitivity for better performance in colourimetric sensing applications. Yellow (H = 30 – 90) and red (H = 330 – 30) colours do not produce a significant enhancement in ΔE for burst, yielding 13% and 64% increases, respectively. The similar sensitivities of the nonburst and burst surfaces in the yellow and red Hue regions is attributed to the disappearance of the periodic features present in burst with increasing line spacing.[36] Interestingly, the improvement in sensitivity of the burst colours follows the improvement in Chroma compared to the nonburst colours. These results

suggest that burst purple, (Fig. 10(B)), is the ideal choice for colourimetric sensing applications with a sensitivity of 3.06/nm (2.02/nm for nonburst - ΔE is dimensionless), implying that less than 1 nm of material on the surface is required for the change in colour to be perceived by the human eye. The sensitivity of the coloured surfaces are, however, not linear with increasing alumina thickness. For a film thickness of 90 nm, the sensitivity of the purple colours drops to 0.56/nm and 0.30/nm for burst and nonburst, respectively, requiring about ~2 nm of material to produce a perceivable change in colour. Blue colours are observed to change the least with increasing film thickness.

Interestingly, while blue surfaces do not perform well as a colourimetric sensor, the surface is best as a radiometric sensor, see Fig. 5. For the blue surfaces, the highest sensitivities observed are for the resonant features identified as $F_{nb,1,blue}$ and $F_{b,2,blue}$ yielding 2.58 and 3.19 nm/nm for the nonburst and burst cases, respectively. These sensitivities rival sensors fabricated via nanolithography techniques. For the purple cases, the features producing the highest sensitivities are $F_{nb,4,purple}$ and $F_{b,4,purple}$ yielding 0.63 nm/nm and 1.02 nm/nm. The sensitivity of the different features identified in the reflectance spectra vary significantly with thickness. For example, $F_{nb,2,blue}$ and $F_{b,3,blue}$ produce sensitivities of 0.31 nm/nm and 0.35 nm/nm, respectively. The plasmon shift, with increasing alumina thickness, is observed to decrease **f**or colours produced with larger line spacings (*i.e.* lower nanoparticle densities – blue to yellow) making the blue colours better for radiometric sensing. Additionally, while the current colours were chosen because they were esthetically pleasing to the eye, colours can be produced with marking speeds as fast as 3000 mm/s making this process viable for industrial applications and the marking of large surface areas. Furthermore, while silver cannot be used directly in biosensing applications due to its reactivity, a thin passivation layer could be formed by ALD on the surface.

4 Conclusion

Colour palettes produced on the surface of silver using nonburst and burst colouring methods were modified by alumina films produced via ALD. The colour and reflectance changes were characterized as a function of alumina film thickness. For burst, the colours first degrade with increasing film thickness but recover at larger thicknesses and the colour range is expanded, whereas for nonburst the colours keep degrading. Underlying periodic structures specific to burst are responsible for this behavior. FDTD modeling of representative surfaces, including a conformal alumina layer, helps explain the colour rotation and recovery observed in experiments with increasing alumina thickness. For alumina thicknesses smaller than the nanoparticle gaps, the changes in the perceived colours are due to the perturbation of plasmonic resonances. For alumina thicknesses larger than the nanoparticle gap, the change in colours originates primarily from the complex reflectance response of the alumina coated structures and modification of the refractive index for grating coupling.

Additionally, the surfaces are thought to be good candidates for colourimetric sensing. The sensitivity of the surfaces depend on the initial colour prior to deposition. The colourimetric response of the burst surfaces are increased by up to 96% relative to the nonburst surfaces. The purple colours are the most sensitive, yielding a sensitivity of 3/nm, which implies that less than 1 nm of alumina is needed to produce a colour shift perceivable by the human eye. The coloured surfaces could also perform well as radiometric sensors, yielding sensitivies as high as 3.19 nm/nm for the blue colours. The ability to tune the structures for grating-assisted coupling and improve colours using burst makes laser-written surfaces very versatile for specific sensing application.

Acknowledgements: We acknowledge the Royal Canadian Mint, the Natural Sciences and Engineering Council of Canada, the Canada Research Chairs program, the Southern Ontario Smart Computing Innovation Platform (SOSCIP), and SciNet. We would like to also acknowledge Dr. Jaspreet Walia, Dr. Fabio Variola and Maël Chow-Cloutier at the University of Ottawa.

References

[1] C. Zhu, G. Yang, H. Li, D. Du, and Y. Lin, “Electrochemical Sensors and Biosensors Based on Nanomaterials and Nanostructures,” *Analytical Chemistry*, vol. 87, pp. 230–249, 2015.

[2] L. E. Kreno, K. Leong, O. K. Farha, M. Allendorf, R. P. V. Duyne, and J. T. Hupp, “Metal-Organic Framework Materials as Chemical Sensors,” *Chemical Reviews*, vol. 112, pp. 1105–1125, 2011.

[3] X. Xu, B. Peng, D. Li, J. Zhang, L. M. Wong, Q. Zhang, S. Wang, and Q. Xiong, “Flexible Visible - Infrared Metamaterials and Their Applications in Highly Sensitive Chemical and Biological Sensing,” *Nano Letters*, vol. 11, pp. 3232–3238, 2011.

[4] J. N. Anker, W. P. Hall, O. Lyandres, N. C. Shah, J. Zhao, and R. P. V. Duyne, “Biosensing with plasmonic nanosensors,” *Nature Materials*, vol. 7, pp. 442–453, 2008.

[5] A. V. Kabashin, P. Evans, S. Pastkovsky, W. Hendren, G. A. Wurtz, R. Atkinson, R. Pollard, V. A. Podolskiy, and A. V. Zayats, “Plasmonic nanorod metamaterials for biosensing,” *Nature Materials*, vol. 8, pp. 867–871, 2009.

[6] J. Walia, J.-M. Guay, O. Krupin, F. Variola, P. Berini, and A. Weck, “Visible light driven plasmonic photochemistry on nano-textured silver,” *Physical Chemistry Chemical Physics*, vol. 20, no. 1, pp. 238–246, 2018.

[7] C. Kim and H. Lee, “Light-assisted surface reactions on metal nanoparticles,” *Catalysis Science & Technology*, vol. 8, pp. 3718–3727, 2018.

[8] Y. Zhang, S. He, W. Guo, Y. Hu, J. Huang, J. R. Mulcahy, and W. D. Wei, “Surface-Plasmon-Driven Hot Electron Photochemistry,” *Chemical Reviews*, vol. 118, pp. 2927–2954, 2018.

[9] A. Y. Vorobyev and C. Guo, “Direct femtosecond laser surface nano/microstructuring and its applications,” *Laser & Photonics Reviews*, vol. 7, no. 3, pp. 385–407, May 2013.

[10] P. Fan, M. Zhong, L. Li, P. Schmitz, C. Lin, J. Long, and H. Zhang, “Sequential color change on copper surfaces via micro/nano structure modification induced by a picosecond laser,” *Journal of Applied Physics*, vol. 114, no. 8, p. 083518, Aug. 2013.

[11] P. Fan, M. Zhong, L. Li, P. Schmitz, C. Lin, J. Long, and H. Zhang, “Angle-independent colorization of copper surfaces by simultaneous generation of picosecond-laser-induced nanostructures and redeposited nanoparticles,” *Journal of Applied Physics*, vol. 115, no. 12, p. 124302, Mar. 2014.

[12] J.-M. Guay, A. Cala, G. Côté, M. Charron, D. Poitras, L. Ramunno, P. Berini, and A. Weck, “Laser-induced plasmonic colours on metals,” *Nature Communications*, vol. 8, p. 16095, 2017.

[13] J. S. Clausen, E. Hø jlund-nielsen, A. B. Christiansen, S. Yazdi, M. Grajower, H. Taha, U. Levy, A. Kristensen, and N. A. Mortensen, “Plasmonic Metasurfaces for Coloration of Plastic Consumer Products,” *Nano Letters*, vol. 14, no. 8, pp. 4499–4504, 2014.

[14] L. Duempelmann, D. Casari, A. Luu-Dinh, B. Gallinet, and L. Novotny, “Color Rendering Plasmonic Aluminum Substrates with Angular Symmetry,” *ACS Nano*, vol. 9, no. 12, pp. 12383–12391, 2015.

[15] A. Kristensen, J. K. W. Yang, S. I. Bozhevolnyi, S. Link, P. Nordlander, N. J. Halas, and N. A. Mortensen, “Plasmonic colour generation,” *Nature Reviews Materials*, vol. 2, p. 16088, Nov. 2016.

[16] X. Duan, S. Kamin, and N. Liu, “Dynamic plasmonic colour display,” *Nature Communications*, vol. 8, no. 14606, pp. 1–9, 2017.

[17] J.-M. Guay, G. Killaire, P. G. Gordon, S. T. Barry, P. Berini, and A. Weck, “Passivation of Plasmonic Colors on Bulk Silver by Atomic Layer Deposition of Aluminum Oxide,” *Langmuir*, vol. 34, no. 17, pp. 4998–5010, 2018.

[18] J. P. Camden, J. A. Dieringer, J. Zhao, and R. P. Van Duyne, “Controlled Plasmonic Nanostructures for Surface-Enhanced Spectroscopy and Sensing,” *Accounts of Chemical Research*, vol. 41, no. 12, pp. 1653–1661, 2008.

[19] A. J. Haes, C. L. Haynes, A. D. Mcfarland, G. C. Schatz, R. P. Van Duyne, and S. Zou, “Plasmonic Materials for Surface-Enhanced Sensing and,” *MRS Bulletin*, vol. 30, pp. 368–375, 2005.

[20] G. Mie, “Beiträge zur Optik trüber Medien, speziell kolloidaler Metallösungen,” *Annalen Der Physik*, no. 28, pp. 377–445, 1908.

[21] W. Doyle, “Optical properties of a suspension of metal spheres.,” *Physical review. B, Condensed matter*, vol. 39, no. 14, pp. 9852–9858, May 1989.

[22] W. a. Murray and W. L. Barnes, “Plasmonic Materials,” *Advanced Materials*, vol. 19, no. 22, pp. 3771–3782, Nov. 2007.

[23] U. Cvelbar, K. K. Ostrikov, A. Drenik, and M. Mozetic, “Nanowire sensor response to reactive gas environment,” *Applied Physics Letters*, vol. 92, p. 133505, 2008.

[24] F. Tam, C. Moran, and N. Halas, “Geometrical Parameters Controlling Sensitivity of Nanoshell Plasmon Resonances to Changes in Dielectric Environment,” *Journal of Physical Chemistry B*, vol. 108, pp. 17290–17294, 2004.

[25] G. Raschke, S. Brogl, A. S. Susha, A. L. Rogach, T. A. Klar, J. Feldmann, B. Fieres, N. Petkov, T. Bein, A. Nichtl, and K. Kurzinger, “Gold Nanoshells Improve Single Nanoparticle Molecular Sensors,” *Nano Letters*, vol. 4, no. 10, pp. 1853–1857, 2004.

[26] N. Liu, M. Mesch, T. Weiss, M. Hentschel, and H. Giessen, “Infrared Perfect Absorber and Its Application As Plasmonic Sensor,” *Nano Letters*, vol. 10, pp. 2342–2348, 2010.

[27] A. N. Shipway, E. Katz, and I. Willner, “Nanoparticle Arrays on Surfaces for Electronic , Optical , and Sensor Applications **,” *Chemical Physical Chemistry*, vol. 1, pp. 18–52, 2000.

[28] K. Kumar, H. Duan, R. S. Hegde, S. C. W. Koh, J. N. Wei, and J. K. W. Yang, “Printing colour at the optical diffraction limit.,” *Nature Nanotechnology*, vol. 7, no. 9, pp. 557–61, Sep. 2012.

[29] A. S. Roberts, A. Pors, O. Albrektsen, and S. I. Bozhevolnyi, “Subwavelength Plasmonic Color Printing Protected for Ambient Use,” *Nano Letters*, vol. 14, no. 2, pp. 783–787, 2014.

[30] S. J. Tan, L. Zhang, D. Zhu, X. M. Goh, Y. M. Wang, K. Kumar, C. Qiu, and J. K. W. Yang, “Plasmonic Color Palettes for Photorealistic Printing with Aluminum Nanostructures,” *Nano Letters*, vol. 14, no. 7, pp. 4023–4029, 2014.

[31] F. Cheng, J. Gao, L. Stan, D. Rosenmann, D. Czaplewski, and X. Yang, “Aluminum plasmonic metamaterials for structural color printing,” *Optics Express*, vol. 23, no. 11, pp. 23279–23285, 2015.

[32] J. Liu and Y. Lu, “Fast Colorimetric Sensing of Adenosine and Cocaine Based on a General Sensor Design Involving Aptamers and Nanoparticles,” *Angewandte Chemie*, vol. 118, pp. 96–100, 2006.

[33] J.-M. Guay, G. Killaire, P. G. Gordon, S. T. Barry, P. Berini, and A. Weck, “Passivation of Plasmonic Colors on Bulk Silver by Atomic Layer Deposition of Aluminum Oxide,” *Langmuir*, vol. 34, no. 17, pp. 4998–5010, 2018.

[34] J. E. Sipe, J. F. Young, and J. S. Preston, “Laser-induced periodic surface structure. I. Theory,” *Physical Review B*, vol. 27, no. 2, 1983.

[35] M. Huang, F. Zhao, Y. Cheng, N. Xu, and Z. Xu, “Origin of laser-induced near-subwavelength ripples: interference between surface plasmons and incident laser,” *ACS Nano*, vol. 3, no. 12, pp. 4062–70, Dec. 2009.

[36] J.-M. Guay, A. Calà Lesina, J. Baxter, G. Killaire, L. Ramunno, P. Berini, and A. Weck, “Topography tuning for plasmonic colour enhancement via picosecond laser bursts,” *Advanced Optical Materials*, p. 1800189, 2018.

[37] J.-M. Guay and et Al., “Enhanced plasmonic coloring of silver and formation of large laser-induced periodic surface structures using multi-burst picosecond pulses,” pp. 1–8, 2016.

[38] J. Jandeleit, G. Urbasch, H. D. Hoffmann, H.-G. Treusch, and E. W. Kreutz, “Picosecond laser ablation of thin copper films,” *Applied Physics A: Materials Science & Processing*, vol. 63, no. 2, pp. 117–121, 1996.

[39] R. A. Waldo, “An Iteration Procedure to Calculate Film Compositions and Thicknesses in Electron-Probe Microanalysis,” in *Microbeam Analysis*, D. E. Newbury, Ed. San Francisco Press, 1988, pp. 310–314.
[40] F. Bunting, *The COLORSHOP Color Primer An Introduction to the History of Color , Color Theory , and Color Measurement*. Grandville, Michigan: Light Source Computer Images, Inc., An X-Rite Company, 1998.
[41] H. Yang, M. Liu, and J. Ouyang, “Novel synthesis and characterization of nanosized γ -Al2O3 from kaolin,” *Applied Clay Science*, vol. 47, pp. 438–443, 2010.
[42] M. Fedel and F. Deflorian, “Electrochemical characterization of atomic layer deposited Al2O3 coatings on AISI 316L stainless steel,” *Electrochimica Acta*, vol. 203, pp. 404–415, 2016.
[43] W. H. Qi and M. P. Wang, “Size and shape dependent melting temperature of metallic nanoparticles,” *Materials Chemistry and Physics*, vol. 88, pp. 280–284, 2004.
[44] W. Luo, W. Hu, and S. Xiao, “Size Effect on the Thermodynamic Properties of Silver Nanoparticles,” *J. Phys. Chem. C*, pp. 2359–2369, 2008.
[45] R. Boidin, T. Halenkovic, V. Nazabal, L. Benes, and P. Nemec, “Pulsed laser deposited alumina thin films,” *Ceramics International*, vol. 42, no. 1, pp. 1177–1182, 2016.
[46] M. D. Groner, F. H. Fabreguette, J. W. Elam, and S. M. George, “Low-Temperature Al2O3 Atomic Layer Deposition,” *Chemistry of Materials*, no. 16, pp. 639–645, 2004.
[47] S. M. George, “Atomic Layer Deposition : An Overview,” *Chemical Reviews*, vol. 110, no. 1, pp. 111–131, 2010.
[48] A. C. Lesina, A. Vaccari, P. Berini, and L. Ramunno, “On the convergence and accuracy of the FDTD method for nanoplasmonics,” *Optics Express*, vol. 23, no. 8, pp. 10481–10497, Apr. 2015.